



Ning Liu · Li-Yun Fu · Gang Tang · Yue Kong · Xiao-Yi Xu

Modified LSM for size-dependent wave propagation: comparison with modified couple stress theory

Received: 12 June 2019 / Revised: 11 November 2019 / Published online: 1 January 2020
© Springer-Verlag GmbH Austria, part of Springer Nature 2020

Abstract A modified LSM is proposed by introducing an independent micro-rotational inertia, which may help characterize the scale-dependent effect and avoid the Poisson's ratio limitation of regular triangle lattices in two dimensions. For this method, some factors may affect data pickup and modeling accuracy, but the 'optimal' inputs, like stiffness ratio, numerical damping, and micro-rotational inertia, could be obtained from parameter identification by the Dakota toolkit (Adams et al., Tech Rep SAND2010–2183, 2009), when a suitable excitation source function and lattice spacing are set up. By comparing with the modified couple stress theory, we analyze the dispersion relationship of elastic waves for the estimation of the characteristic material length. It shows that this modified LSM may provide an alternative and promising way to investigate the size-dependent wave propagation in elastic media numerically.

1 Introduction

Conventional continuum mechanics treats matter to be continuously distributed throughout a body [48]. It provides a reasonable assumption for analyzing the macroscale behavior of materials by ignoring size-dependent effects [28]. However, experimental investigations imply a size-dependent mechanical behavior for microscale structures [33, 57]. Solid materials can be regarded as an assembly of microstructural elements that interact with each other by microstructural forces. Generally, the modeling of the mechanical behaviors of such a representation may be divided into two categories [48]. The former is based on the concepts of stress and strain, where the governing equations are formulated by introducing extra elastic constants to characterize the

N. Liu · G. Tang (✉)
College of Mechanical and Electrical Engineering, Beijing University of Chemical Technology, Beijing 100029, China
E-mail: tanggang@mail.buct.edu.cn

L.-Y. Fu (✉)
Key Laboratory of Deep Oil and Gas, China University of Petroleum (East China), Qingdao 266580, Shandong, China
E-mail: lfu@upc.edu.cn

Y. Kong
School of Aeronautic Science and Engineering, Beihang University, Beijing 100083, China

X. Xu
State Key Laboratory of Ore Deposit Geochemistry, Institute of Geochemistry, Chinese Academy of Sciences, Guiyang 550081, China

X. Xu
University of Chinese Academy of Sciences, Beijing 100049, China

size-dependent effects. The latter is a discrete-based model, for which equilibrium, kinematic, and constitutive equations are generated for each microstructural element and the corresponding microstructural force [48].

Enhanced continuum theory, which considers the size-dependent effects, was first developed by the Cosserats [5], but the concept of ‘couple stress’ was originally postulated by Voigt [51]. The Cosserat theory (or micro-polar theory) is formulated by introducing extra rotational degrees of freedom, in order to analyze materials with couple stress [5]. Later, in Toupin’s view [50], the rotation in the classical micro-polar elasticity is not independent but constrained to match the rotation of the deformation gradient. Then, with Mindlin and Tiersten [38] and Koiter [26], the classical couple stress theory, also called the indeterminate couple stress theory in the literature [10], is elaborated. This theory contains two extra higher-order characteristic coefficients in addition to the two classical Lamé constants for isotropic elastic materials in its constitutive equation [16]. Yang et al. [60] proposed a modified couple stress theory, in which the couple stress material parameters for linear isotropic elastic material are reduced from two to just one by introducing an equilibrium equation for the moment of couples. This feature makes it unlike those in the classical couple stress theory. Subsequently, Park and Gao [45] provided a variational formulation of this modified couple stress theory. This theory is widely used to study bending, buckling, post-buckling, linear and nonlinear vibration problems related to microbeams [34,44,53], rod [17,62], and microplates [11,35,54], to investigate the nonlocal longitudinal stress waves propagation [15,45], and to characterize the size-dependent propagation of one-dimensional elastic stress waves in a functionally graded nanoscale bar [25] and a shear deformable nanobeam [2].

Compared with the generalized continuum theories capable of capturing size-dependent effects, the discrete-based approaches have a considerable advantage: inhomogeneous effects at the micro-level could be captured [48]. Discrete-based methods, such as molecular dynamics (MD), the discrete element method (DEM), and the lattice spring model (LSM), have been used to simulate wave propagation through a piece of rocks by a particle-based model [49], Rayleigh waves by an elastic lattice model [9], and seismic waveforms [27] in heterogeneous media. In particular, strong shock waves propagating in dense deuterium have been simulated by molecular dynamics [30]. Between these different numerical methods, LSM attracts the most interest, since it can bridge a gap between the continuous and discontinuous modeling by emulating the continuous materials in a discrete way [46]. LSM is based on the atomic lattice structure of materials, where the material is represented by a system of discrete units interacting via springs or beams [41]. In some references [19,41,46], LSM is called discrete element method as well, but different from the DEM derived by Cundall [6], in which the material is modeled by rigid blocks connected by springs at their contact surfaces. In the earlier LSMs, the lattice nodes are only composed of normal springs, and the Poisson’s ratio is fixed at 0.25 in three dimensions and $\frac{1}{3}$ for the two-dimensional case [64] for triangular lattices. Later, some researchers [7,13,24,66] introduced a non-central shear-type spring, which could emulate different Poisson’s ratios, but with an upper bound of 0.25 for 3D, or $\frac{1}{3}$ for 2D. Meanwhile, some other advanced models have been developed as well, like the multibody shear spring [39,42], the beam element model [23,29,31,47], the Born spring model [3], the nonlocal potential spring model [20], and the distinct lattice spring model (DLSM) [22,65]. Those high-order LSMs are attempted to tackle the Poisson’s ratio limitation existing in conventional LSMs.

The LSM with non-central shear springs not only introduces shear displacements but also rotational degrees of freedom, which seems to be similar to the concepts of micro-polar medium. This may imply that this model could be used to study the size-dependent effects and also to represent the material with a higher Poisson’s ratio. Suiker et al. [48] studied the former by a comparison with the Cosserat continuum model, in which the lattice nodes are seen as circular disks with a micro-rotational inertia of $\frac{1}{8}md^2$. As LSM differs from the DEM proposed by Cundall [6], whose elements interact through the contact surfaces, we might be able to regard the micro-rotational inertia as independent of lattice spacing. Therefore, we propose a modified LSM by introducing an independent micro-rotational inertia. This coefficient as an input could be obtained by the parameter identification process provided in the Dakota toolkit [1] for a given material.

The aim of this paper is to demonstrate that this modified LSM can be used to analyze and characterize the size-dependent effect on wave propagation in an elastic medium with a higher Poisson’s ratio by comparison with the modified couple stress theory. The remaining parts of this paper are organized as follows: In Sect. 2, the wave motion of the modified couple stress theory is reviewed and derived; in Sect. 3, the algorithm of the modified LSM is briefly outlined, including the governing equations (Sect. 3.1); some factors may affect data pickup and modeling accuracy, like source functions (Sect. 3.2), numerical damping (Sect. 3.3), lattice spacing (Sect. 3.4), micro-rotational inertia (Sect. 3.5), and parameter identification for the ‘optimal’ inputs by the Dakota toolkit (Sect. 3.6); in Sect. 4, the implementation of LSM for modeling elastic wave propagation is validated and verified by a commercial finite element software (Nastran); in Sect. 5, we compare elastic

wave dispersions between the modified LSM modeling and the corresponding theoretical predictions; the conclusions and the future work are summarized in Sect. 6.

2 Wave equations of modified couple stress theory

2.1 Governing equations

Concerning the modified couple stress theory proposed by Yang et al. [60], the elastic strain energy Π occupying a volume V is given by

$$\Pi = \int_V w dV = \frac{1}{2} \int_V (\boldsymbol{\sigma} : \boldsymbol{\varepsilon} + \mathbf{m} : \boldsymbol{\chi}) dV, \quad (1)$$

where w , $\boldsymbol{\sigma}$, $\boldsymbol{\varepsilon}$, \mathbf{m} , and $\boldsymbol{\chi}$ are the elastic energy density, the Cauchy stress tensor, the strain tensor, the symmetric curvature tensor, and the deviatoric part of the couple stress tensor, respectively. In the Cartesian coordinate system, for an isotropic linear elastic material, the constitutive and geometric equations can be written as

$$\boldsymbol{\sigma} = \lambda \text{tr}(\boldsymbol{\varepsilon}) \mathbf{I} + 2\mu \boldsymbol{\varepsilon}, \quad (2)$$

$$\boldsymbol{\varepsilon} = \frac{1}{2} (\nabla \mathbf{u} + (\nabla \mathbf{u})^T), \quad (3)$$

and

$$\mathbf{m} = 2l^2 \mu \boldsymbol{\chi}, \quad (4)$$

$$\boldsymbol{\chi} = (\nabla \boldsymbol{\theta} + (\nabla \boldsymbol{\theta})^T), \quad (5)$$

where λ and μ are Lamé constants in the classical continuum theory and l is the square root of the ratio of the curvature modulus to the shear modulus as an additional material parameter to characterize the size dependence. This characteristic material length can be determined from bending or torsion tests [4]. The rotation vector $\boldsymbol{\theta}$ is related to the displacement vector \mathbf{u} defined as

$$\boldsymbol{\theta} = \frac{1}{2} \text{curl}(\mathbf{u}). \quad (6)$$

Summarily, there are two main differences between the modified couple stress theory and the classical couple stress theory: The couple stress tensor of the former becomes symmetric by introducing an equilibrium equation for the moment of couples, which reduces the number of the couple stress parameters in addition to the conventional Lamé's constants from two to just one [34, 44, 52]. These features make the modified couple stress theory easier to use.

2.2 Wave motion equations

Taking Eqs. (1–6) into the linear and angular equilibrium equations of an infinitesimal element of material, based on the virtual work theorem and integrated with Newton's second law, we obtain the linear equilibrium equation [18]

$$(\lambda + \mu + l^2 \mu \nabla^2) \nabla(\nabla \mathbf{u}) + (\mu - l^2 \mu \nabla^2) \nabla^2 \mathbf{u} + \rho \mathbf{F} = \rho \frac{\partial^2 \mathbf{u}}{\partial t^2}, \quad (7)$$

where \mathbf{F} is the body force vector and ρ is the density. This relation has been derived previously by Mindlin and Tiersten [38] within the context of the classical couple stress theory, while the Mindlin–Tiersten formulation involved two couple stress parameters [18], instead of only one characteristic material length l in this modified couple stress theory.

In Eq. (7), the body force term consists of a gravity term and a source term. The gravity term is significant at low frequencies in normal mode seismology. However, it can be neglected in the surface wave propagation. Here, we don't take the body force into consideration and could get the displacement equation of motion

$$(\lambda + \mu + l^2 \mu \nabla^2) \nabla(\nabla \mathbf{u}) + (\mu - l^2 \mu \nabla^2) \nabla^2 \mathbf{u} = \rho \frac{\partial^2 \mathbf{u}}{\partial t^2}. \quad (8)$$

With reference to the vector field theory where any vector can be represented by a sum of a gradient of scalar Φ and a curl of vector Ψ , the displacement field \mathbf{u} can be written as follows:

$$\mathbf{u} = \nabla \Phi + \nabla \times \Psi, \quad \nabla \Psi = 0. \quad (9)$$

Substituting Eq. (9) into Eq. (8), we can obtain

$$\rho \frac{\partial^2}{\partial t^2} (\nabla \Phi + \nabla \times \Psi) = (\lambda + \mu + \eta \nabla^2) \nabla [\nabla(\nabla \Phi + \nabla \times \Psi)] + (\mu - \eta) \nabla^2 (\nabla \Phi + \nabla \times \Psi), \quad (10)$$

where

$$\eta = l^2 \mu; \quad (11)$$

$$\nabla \cdot (\nabla \Phi) = \nabla^2 \Phi, \quad (12)$$

$$\nabla \cdot (\nabla \times \Psi) = 0, \quad (13)$$

$$\frac{\partial^2}{\partial t^2} (\nabla \Phi) = \nabla \frac{\partial^2 \Phi}{\partial t^2}, \quad (14)$$

$$\nabla^2 (\nabla \Phi) = \nabla (\nabla^2 \Phi); \quad (15)$$

and

$$\nabla^2 (\nabla \times \Psi) = \nabla \times (\nabla^2 \Psi), \quad (16)$$

$$\frac{\partial^2}{\partial t^2} (\nabla \times \Psi) = \nabla \times \left(\frac{\partial^2 \Psi}{\partial t^2} \right). \quad (17)$$

Then, Eq. (10) becomes

$$\nabla \left((\lambda + \mu + \eta \nabla^2 + \mu - \eta \nabla^2) \nabla^2 \Phi - \rho \frac{\partial^2 \Phi}{\partial t^2} \right) + \nabla \times \left((\mu - \eta \nabla^2) \nabla^2 \Psi - \rho \frac{\partial^2 \Psi}{\partial t^2} \right) = 0. \quad (18)$$

Therefore, we obtain

$$(\lambda + \mu + \eta \nabla^2 + \mu - \eta \nabla^2) \nabla^2 \Phi = \rho \frac{\partial^2 \Phi}{\partial t^2}, \quad (19)$$

namely

$$(\lambda + 2\mu) \nabla^2 \Phi = \rho \frac{\partial^2 \Phi}{\partial t^2}; \quad (20)$$

and

$$(\mu - \eta \nabla^2) \nabla^2 \Psi = \rho \frac{\partial^2 \Psi}{\partial t^2}. \quad (21)$$

Equation (20) denoted by the scalar potential is the wave motion equation of the irrotational field, the same as that in the classical continuum theory. It may mean that the dilatation wave is non-dispersive. Equation (21) can be named as the rotational wave motion equation represented by vector potential, which seems to be influenced by couple stress.

We assume that Φ and Ψ can be written in the form of plane harmonic waves with amplitudes and phases varying in space and time,

$$(\Phi, \Psi) = (a, \mathbf{A}) \exp [i \mathbf{k} \cdot (\mathbf{x} - \mathbf{c}t)] = (a, \mathbf{A}) \exp (i \mathbf{k} \mathbf{x} - i \omega t), \quad (22)$$

where a , \mathbf{A} , \mathbf{k} , ω , and \mathbf{c} are the amplitude of Φ , the amplitude vector of Ψ , the wave vector, angular frequency, and phase velocities, respectively. In Eq. (22),

$$\mathbf{k} = k\mathbf{n}, \quad (23)$$

where k is the wave number and \mathbf{n} is the unit wave normal. The wave vector \mathbf{k} is related to the vector wavelengths $\mathbf{\Lambda}$ by the scalar product

$$\mathbf{k}\mathbf{\Lambda} = 2\pi \quad (24)$$

and is also related to the vector of phase velocities \mathbf{c} by

$$\mathbf{k}\mathbf{c} = \omega. \quad (25)$$

Taking Eq. (22) into Eqs. (20) and (21), when $a \neq 0$, we find

$$c_1^2 = \frac{\lambda + 2\mu}{\rho}; \quad (26)$$

$$(\mu k^2 + \eta k^4 - k^2 c_2^2 \rho) \mathbf{\Lambda} = 0. \quad (27)$$

Because $\mathbf{\Lambda} \neq \mathbf{0}$, we have

$$\mu k^2 + \eta k^4 - k^2 c_2^2 \rho = 0. \quad (28)$$

When $k^2 \neq 0$, we attain

$$c_2^2 = \frac{\mu + \eta k^2}{\rho} = \frac{\mu}{\rho} (1 + l^2 k^2). \quad (29)$$

From this equation, we could see that c_2 is related to the wave number k . It also can be given by

$$c_2 = c_2^0 \sqrt{1 + l^2 k^2}, \quad (30)$$

where

$$c_2^0 = \sqrt{\frac{\mu}{\rho}}. \quad (31)$$

With

$$\omega^2 = k^2 (c_2^0)^2 (1 + l^2 k^2), \quad (32)$$

we solve Eq. (32) for k^2 and get the two roots

$$k_1^2 = \frac{1}{2} l^{-2} \left(\sqrt{1 + \frac{4l^2 \omega^2}{(c_2^0)^2}} - 1 \right) \quad (33)$$

and

$$k_2^2 = -\frac{1}{2} l^{-2} \left(\sqrt{1 + \frac{4l^2 \omega^2}{(c_2^0)^2}} + 1 \right). \quad (34)$$

Because l is a real number, one of the two roots is a real, and the other is a pure imaginary. Hence, it could be said that there are two rotational waves: One propagates, and the other does not. Both are related to the angular frequency, suffering dispersion.

The wave with a real wave number is called as a real wave. Its group velocity is defined by

$$c_g = \frac{d\omega}{dk_1} = \frac{c_2^0 (1 + 2l^2 k_1^2)}{\sqrt{1 + l^2 k_1^2}}, \quad (35)$$

which increases monotonically with respect to lk_1 . Based on this phenomenon, it might make the couple stress effect detectable in high-frequency vibrations. When the value of the characteristic material constant l is small compared to that of the wavelength, the impact caused by couple stress could be ignored, and the group velocity is approximately the same. The phase velocity of the real wave increases monotonically with increasing lk_1 . When

$$lk_1 = \sqrt{\frac{\lambda + \mu}{\mu}}, \tag{36}$$

the real wave velocity reaches that of the dilatational wave c_1 .

2.3 Elastic wave velocities

To simplify numerical analyses, the velocity of the real rotational wave is dimensionless; by dividing the reference shear velocity, the classical shear velocity c_2^0 becomes

$$c_2^* = \frac{c_2}{c_2^0} = \sqrt{1 + l^2 k_1^2}. \tag{37}$$

The dimensionless group velocity, the ratio of the original group velocity to that of classical shear velocity, is written as

$$c_g^* = \frac{1 + 2l^2 k_1^2}{\sqrt{1 + l^2 k_1^2}}. \tag{38}$$

Figure 1 shows log-log plots of the dimensionless phase and group velocities, showing the couple stress effect. We could see that the velocities increase with increasing lk_1 , the product of the characteristic material constant l and the real wave number k_1 . In the classical theory of elastic wave propagation, the compressional and shear wave velocities, c_p and c_s , are given by

$$c_p = \sqrt{\frac{\lambda + 2\mu}{\rho}} \tag{39}$$

and

$$c_s = \sqrt{\frac{\mu}{\rho}}. \tag{40}$$

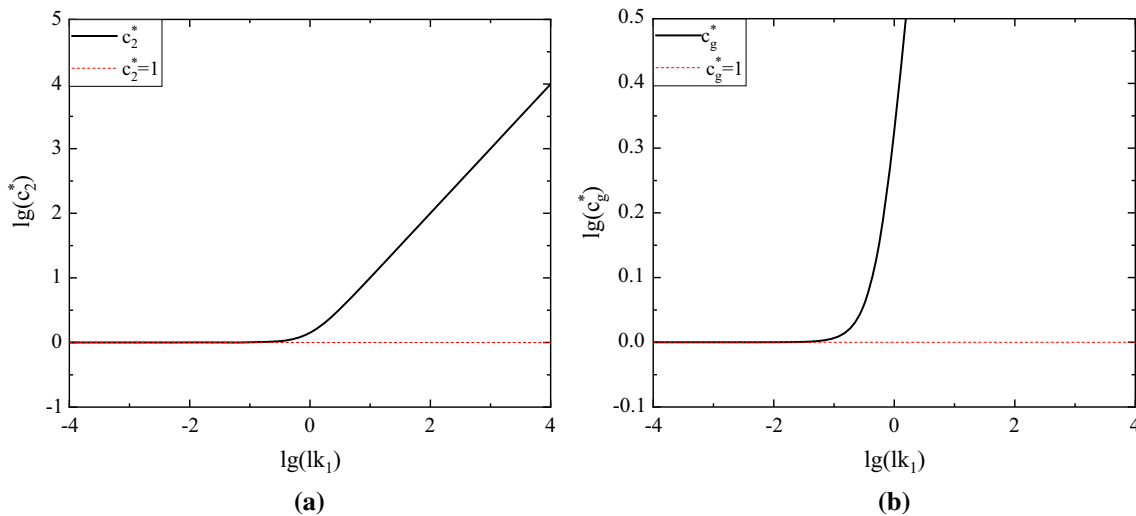


Fig. 1 Dimensionless phase and group velocities changing with respect to lk_1 on the logarithmic scale

Thus, it would say that the shear wave is dispersive due to the couple stress effect from the size dependence. Figure 1b demonstrates the ratio of the group to the classical shear wave velocities varies with lk_1 . When the characteristic material length is zero, it virtually indicates that the couple stress effect is neglected, and we have

$$lk_1 = 0. \quad (41)$$

Then, the behavior of the wave propagation degrades into the classical continuum theory. For this situation, the phase velocity has the following relation:

$$\omega = ck. \quad (42)$$

The group velocity is defined by

$$c_g = \frac{d\omega}{dk}, \quad (43)$$

so we have

$$c_g = c, \quad (44)$$

for isotropic linear elastic media in the classical continuum theory. Based on the traditional continuum elasticity, wave propagation is treated as non-dispersive even for large wave numbers or high vibration frequencies, which differs from the experimental results and shows the limitation of the classical continuum theory. Therefore, it is necessary to develop advanced theories in elasticity for a broader range of applications, e.g., couple stress theory.

3 Elastic wave propagation by the modified LSM

3.1 Modified lattice spring modeling

Lattice spring modeling methods stem from the atomic lattice structure of materials, in which the object is discretized into mass nodes, connecting with normal and shear springs. Assuming that these springs behave in a linear elastic way, the interaction forces between two lattice nodes i and j , including normal force F_n^{ij} and tangential force F_s^{ij} , can be written as

$$F_n^{ij} = K_n u_n^{ij} \quad (45)$$

and

$$F_s^{ij} = K_s u_s^{ij}, \quad (46)$$

where K_n , K_s , u_n^{ij} , and u_s^{ij} are the normal and shear spring stiffness and the distance increments in normal and tangential directions, respectively. The relative displacements u_n^{ij} and u_s^{ij} are calculated in a similar way as expressed in Ref. [48],

$$u_n^{ij} = (\mathbf{u}_i - \mathbf{u}_j) \cdot \mathbf{n}_n^{ij}, \quad (47)$$

$$u_s^{ij} = (\mathbf{u}_i - \mathbf{u}_j) \cdot \mathbf{n}_s^{ij} + \frac{d}{2} (\boldsymbol{\theta}_i + \boldsymbol{\theta}_j) \cdot \mathbf{n}_o^{ij}, \quad (48)$$

$$\mathbf{n}_o^{ij} = \mathbf{n}_n^{ij} \times \mathbf{n}_s^{ij}, \quad (49)$$

where \mathbf{u}_i and \mathbf{u}_j are the coordinate vectors of nodes i and j ; $\boldsymbol{\theta}_i$ and $\boldsymbol{\theta}_j$ are angular coordinate vectors; \mathbf{n}_n^{ij} and \mathbf{n}_s^{ij} are the normal and tangential unit vectors; d is the lattice spacing. Not only the tensile and shear forces but also the torque act on the mass nodes which is represented by

$$M^{ij} = \frac{1}{2} F_s^{ij} \cdot d, \quad (50)$$

where M^{ij} is the moment. The forces and moments acting on every node could be obtained, based on a central difference scheme. The nodal motion [8, 14] is computed as follows:

$$\dot{\mathbf{u}}_i^{(t+\frac{\Delta t}{2})} = \dot{\mathbf{u}}_i^{(t-\frac{\Delta t}{2})} + \frac{\sum \mathbf{F}_i^{(t)} \Delta t}{m}, \quad (51)$$

$$\mathbf{u}_i^{(t+\Delta t)} = \mathbf{u}_i^{(t)} + \dot{\mathbf{u}}_i^{(t+\frac{\Delta t}{2})} \Delta t; \quad (52)$$

and

$$\boldsymbol{\omega}_i^{(t+\frac{\Delta t}{2})} = \boldsymbol{\omega}_i^{(t-\frac{\Delta t}{2})} + \frac{\sum \mathbf{M}_i^{(t)} \Delta t}{I}, \quad (53)$$

$$\boldsymbol{\theta}_i^{(t+\Delta t)} = \boldsymbol{\theta}_i^{(t)} + \boldsymbol{\omega}_i^{(t+\frac{\Delta t}{2})} \Delta t, \quad (54)$$

where \mathbf{F}_i and \mathbf{M}_i are resultant force and moment acting on node i and I is a given micro-rotation inertia. Notably, this parameter from inputs is independent of lattice spacing d , which makes our LSM distinct from the existing LSMs. This modified LSM might be used to characterize the size-dependent effect and will be discussed in the following sections.

In LSM, to ensure the stability of this explicit integration algorithm as displayed in Eqs. (51)–(54), the time step satisfies

$$\Delta t \leq \Delta t_{\text{cr}}, \quad (55)$$

with the critical time step

$$\Delta t_{\text{cr}} = \frac{2}{\omega_{\text{max}}}, \quad (56)$$

where ω_{max} is the largest eigen frequency within the lattice spring network. To dissipate kinetic energy, a non-viscous damping ζ is used to obtain quasi-static solutions [22]. The dissipated force $\Delta \mathbf{G}_{\text{dissipated}}$ of node i could be written as follows:

$$\frac{(\Delta \mathbf{G})_{\text{dissipated}}^i}{\mathbf{G}_i} = -\zeta \text{sgn} \left(\dot{\mathbf{x}}_i^{(t-\frac{\Delta t}{2})} + \frac{\ddot{\mathbf{x}}_i \Delta t}{2} \right) \quad (57)$$

with the generalized forces

$$\mathbf{G} = (\mathbf{F} \mathbf{M})^T \quad (58)$$

and the generalized displacements

$$\mathbf{x} = (\mathbf{u} \boldsymbol{\theta})^T. \quad (59)$$

This dynamic relaxation scheme is proposed by Otter et al. [43] for quasi-static solutions, which is widely used in discrete-based numerical methods, like molecular dynamics (MD) simulations, DEM developed by Cundall [6], discrete lattice spring model (DLSM) [65], and other nonconventional LSM [55]. The entire calculation process for this LSM modeling is illustrated in Fig. 2.

3.2 Source functions

Figure 3 shows a numerical model where a semicircle with the radius of 20 mm represents a quasi-semi-infinite half space. A vertical downward displacement excitation is applied to a lattice node located at the center of the semicircle, with the receivers arranged along the horizontal direction with a spacing of 2.0 mm. There are two commonly used source functions [12, 21, 63]: the cosine function and a Gaussian second-order differential function (namely Ricker wavelet), given by

$$u_z = -A_0 \cos(2\pi ft), \quad 0 \leq t \leq \frac{T}{2}, \quad (60)$$

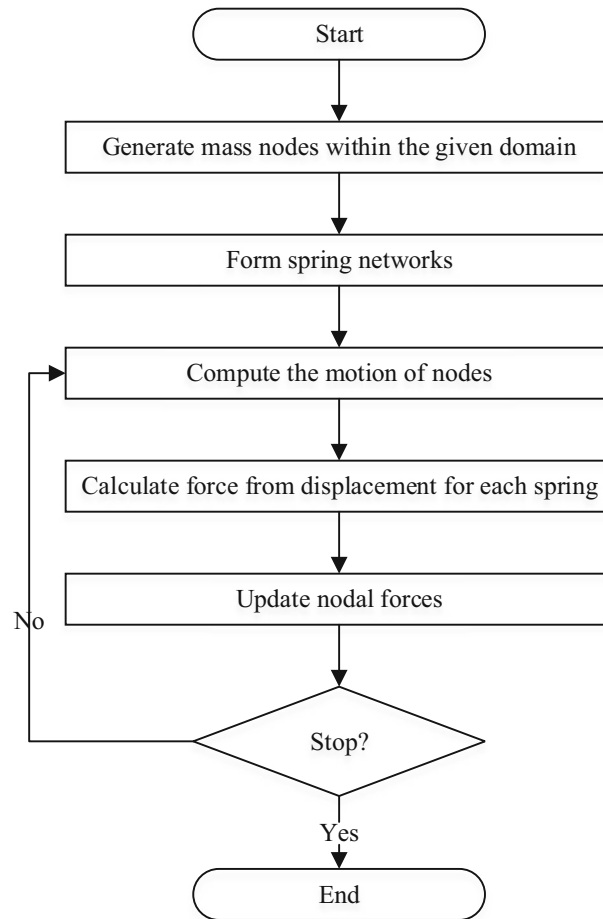


Fig. 2 Flowchart for modified LSM modeling

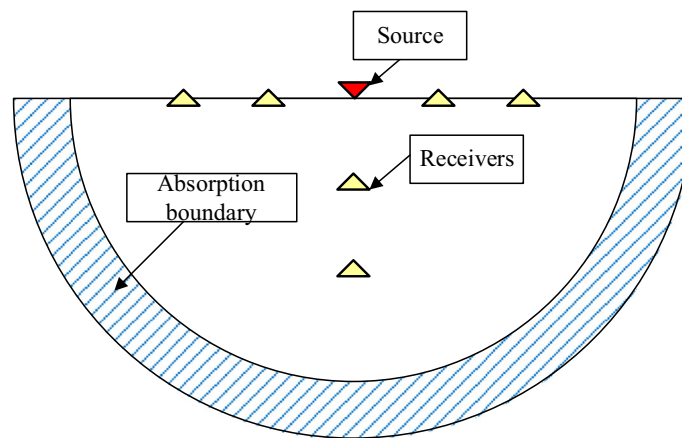


Fig. 3 Numerical model and boundary conditions

and

$$u_z = -A_0 \left(1 - 2\pi^2 f^2 \left(t - \frac{T}{2} \right)^2 \right) \exp \left(-\pi^2 f^2 \left(t - \frac{T}{2} \right)^2 \right), \tag{61}$$

where A_0 , T , and f represent amplitude, period, and frequency, respectively.

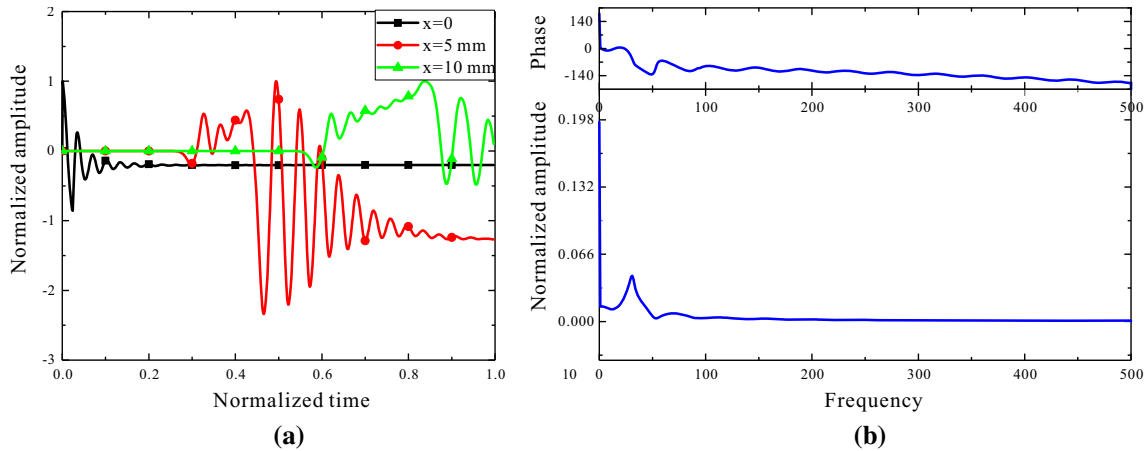


Fig. 4 Time-domain vertical displacements (a) by the cosine function source for the receivers located at 0, 5, and 10 mm from the source and the displacement response spectrum (b) in the frequency domain for the source node at 0.0 mm

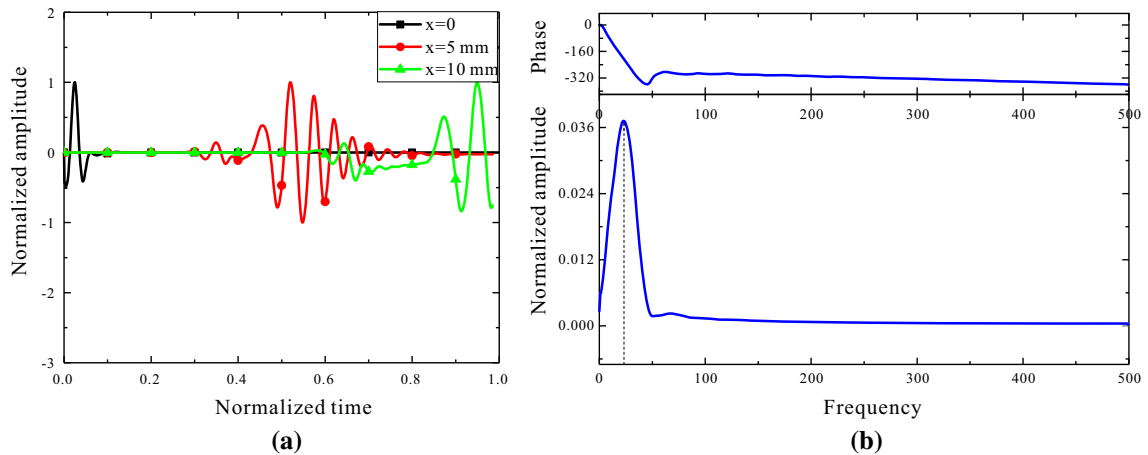


Fig. 5 Time-domain vertical displacements (a) by the Ricker wavelet source for the receivers located at 0, 5, and 10 mm from the source and the displacement response spectrum (b) in the frequency domain for the source node at 0.0 mm

Figure 4a shows the displacement versus time curves for the lattice nodes located at 0, 5, and 10 mm away from the cosine function source within $0 \leq t \leq \frac{T}{2}$. We could see that responses at these nodes still oscillate for a long time after the excitation stops with serious dispersions. These lattice nodes can't maintain initial waveforms well. Each harmonic component propagates at its phase velocity, causing a disordered time-domain response and high-frequency oscillation. The compressional wave velocity is measured with the distance divided by the first arrival time. However, it is difficult to accurately tell the travel time of the shear wave and the corresponding amplitude. Figure 4b shows the fast Fourier transform (FFT) result of the time-domain displacement response for the source node. The normalized spectrum changes largely in amplitude with two sharp peaks.

Figure 5a displays the time-domain responses for these lattice nodes from the Ricker wavelet source, a widely used artificial source of seismic waves. We see that the displacement response for the source node at 0.0 mm can keep the Ricker wavelet waveform well due to lack of the cutoff time. The displacement responses from the other two receivers change with time largely, with some dispersions mainly caused by lattice meshing, which will be discussed in detail in the next section. From the displacement spectra, it is easier to distinguish between P- and S-waves. In Fig. 5b, the corresponding frequency spectrum for the source node at 0.0 mm demonstrates a smooth change in normalized amplitude. In general, the Ricker wavelet is suitable as an artificial source in elastic wave modeling [49].

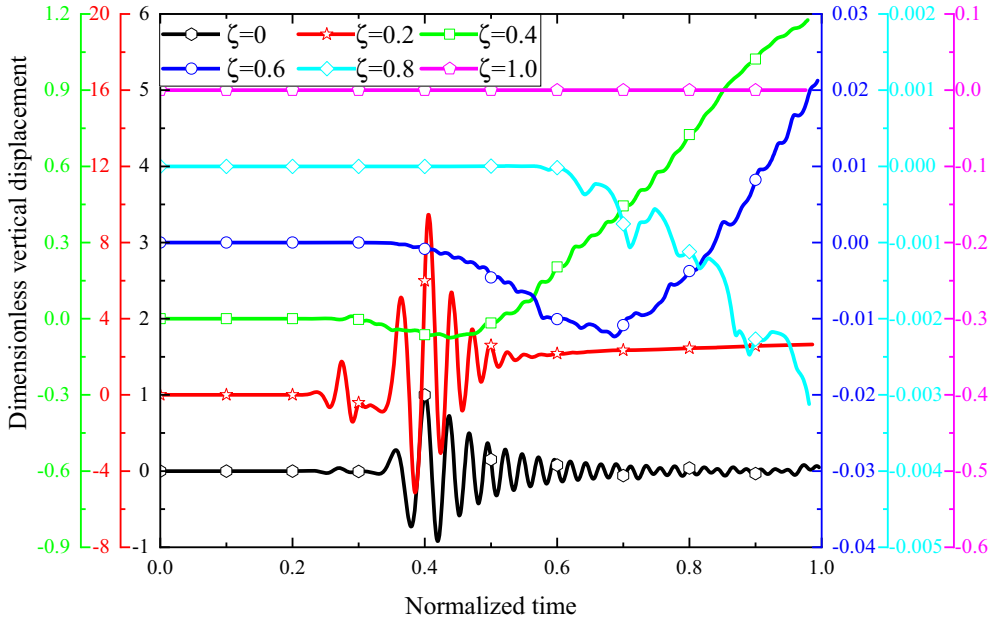


Fig. 6 Vertical displacement responses at 10 mm from the excitation under different numerical damping

3.3 Numerical damping

To dissipate the residual kinetic energy over lattice nodes, a stable numerical solution to Eq. (57) requires artificial numerical damping with optimal values. Figure 6 illustrates the time-domain vertical displacements under different numerical damping for the surface lattice node at 10 mm away from the excitation without micro-rotation. We take a lattice spacing of 0.2 mm in the LSM modeling. We see that the displacement signal without numerical damping ($\zeta = 0$) oscillates for a long time. It is difficult to distinguish these wave types and determine their arrival times. For the damping with $\zeta = 0.4\text{--}0.8$, the resulting signals are attenuated significantly to almost zero in a relatively short period, with the waveforms disordered severely. The corresponding arrival times of P- or S-waves cannot be identified, either. The curve with the numerical damping of $\zeta = 1.0$ indicates that the nodal kinetic energy is completely dissipated, and the lattice node does not move. In conclusion, the optimal numerical damping comes to $\zeta = 0.2$, with the resulting signal stable at a positive value and the P- and S-waveforms keeping well. The stabilized lattice node does not return to its original position. As a result, we could roughly estimate the ideal range of numerical damping (e.g., 0–0.2 for Fig. 6). In general, the numerical damping is not only influenced by time steps but also by lattice spacings. For two-dimensional lattice spring models lack of the micro-polar effect, the optimal damping value is usually 0.1, calibrated by the Dakota toolkit (short for design analysis kit for optimization and terascale applications). It is 0.2 for the models with the given micro-rotational inertia. An identification process of damping values by the Dakota toolkit will be described in detail below.

3.4 Lattice spacing

For the modified LSM, wave velocities depend on kd , the product of lattice spacing d , and wave number k , which is called dispersion relation [48]. Therefore, the meshing sensitivity to the LSM simulation of elastic waves has been discussed [40,48]. Equations (39) and (40) give the expressions of P- and S-wave velocities in the classical theory without the nodal micro-rotation effect. According to the long-wave approximation, $kd \approx 0$, the P- and S-wave velocities could be defined by

$$c_P = \sqrt{\frac{\lambda_{\text{cell}} + 2\mu_{\text{cell}}}{\rho_{\text{cell}}}} \tag{62}$$

and

$$c_S = \sqrt{\frac{\mu_{\text{cell}}}{\rho_{\text{cell}}}}, \quad (63)$$

where λ_{cell} , μ_{cell} , and ρ_{cell} are the corresponding two Lamé constants, and the material density in the lattice unit cell is expressed as follows:

$$\rho_{\text{cell}} = \frac{m_{\text{cell}}}{A_{\text{cell}}}, \quad (64)$$

in which the equivalent mass of the lattice unit cell is equal to that of a lattice node, namely $m_{\text{cell}} = m_{\text{node}}$. The lattice node mass is calculated by

$$m_{\text{node}} = \frac{1}{4} \rho_{\text{input}} \pi d^2, \quad (65)$$

where ρ_{input} is the input value of each lattice node. Based on the equivalence of strain energy stored in a lattice unit cell, the two Lamé constants lead to [41]

$$\lambda = \frac{\sqrt{3} (K_n - K_s)}{4} \quad (66)$$

and

$$\mu = \frac{\sqrt{3} (K_n + K_s)}{4}. \quad (67)$$

Inserting the expressions for λ and μ in Eqs. (62) and (63), we obtain

$$c_P = \sqrt{\frac{3 (3K_n + K_s)}{2\pi \rho_{\text{input}}}}, \quad (68)$$

$$c_S = \sqrt{\frac{3 (K_n + K_s)}{2\pi \rho_{\text{input}}}}, \quad (69)$$

where

$$\rho_{\text{cell}} = \frac{\pi}{2\sqrt{3}} \rho_{\text{input}}. \quad (70)$$

The velocity ratio is

$$\left(\frac{c_P}{c_S}\right)^2 = \frac{3K_n + K_s}{K_n + K_s} = \frac{3 + \xi}{1 + \xi}, \quad (71)$$

where

$$\xi = \frac{K_s}{K_n} \quad (72)$$

is the ratio of the shear to the normal stiffness for all interactions, generally ranging from 0 to 1.0. Equation 71 also could be obtained by the formulation shown in Ref. [48]. Figure 7 shows in the classical LSM how the stiffness ratio affects the velocity ratio. For the LSM without micro-rotation, we could see $\frac{c_P}{c_S} = \sqrt{3}$ when $K_s = 0$. For this case, the two classical Lamé constants are equal to each other, and Eqs. (66) and (67) are same as those expressions in Ref. [41].

To discuss the influence of mesh sizes on the displacement response in the LSM, we choose Ricker wavelet in Eq. (61) as the source function, with $T = 0.5 \mu\text{s}$, $f = 2 \text{ MHz}$, and the time step 10.0 ns for a duration of $10 \mu\text{s}$. Figure 8 shows the vertical displacement responses under different mesh sizes for the node at 10 mm from the source. We see that for the lattice spacing $d \geq 1.0 \text{ mm}$, there appear severe dispersions by the influence of sparse meshing. On the other hand, for small lattice spacings, the stability condition shown in Eqs. (55) and (56) is not easy to satisfy for a given time step. For the presented model, stable response curves can be obtained with $d = 0.08\text{--}0.5 \text{ mm}$, and the P- and S-wave arrival times can be directly identified.

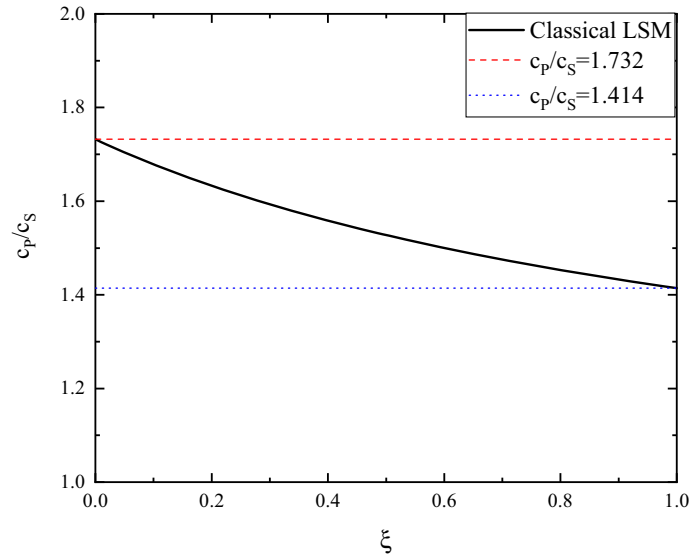


Fig. 7 Velocity ratio changing with respect to stiffness ratio for classical LSM

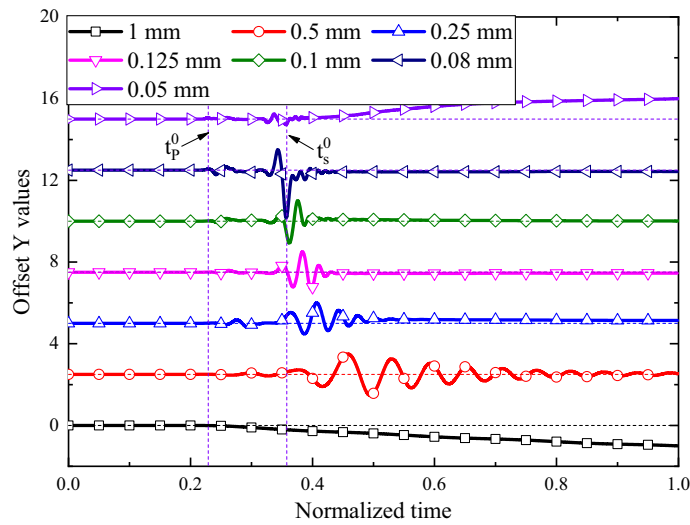


Fig. 8 Vertical displacement responses under different mesh sizes for the node at 10 mm from the source

3.5 Micro-rotation effect

For the lattice model without considering the micro-rotation effect, namely classical LSM, the ratio of P- to S-wave velocities is up to $\sqrt{3}$ according to Eqs. (71) and (72) and Fig. 7, while many metallic materials usually have a Poisson’s ratio higher than 2.0 [36,61]. The micro-rotation effect does affect equivalent elastic parameters of a lattice unit cell. Figure 9 shows the displacement snapshots of LSM in the vertical direction at $t = 4.0 \mu\text{s}$ for the classical and micro-polar media, respectively. Both models have similar inputs except an extra rotational degree of freedom for the micro-polar medium. We see that velocity ratio of P- to S-waves is about 1.63 for the model without rotation effect and raises to 1.93 (higher than the upper limit of velocity ratio for classical LSM $\sqrt{3}$ by 6.13%) by introducing the micro-rotation. For this numerical example, the ratio increases by about 18.41%.

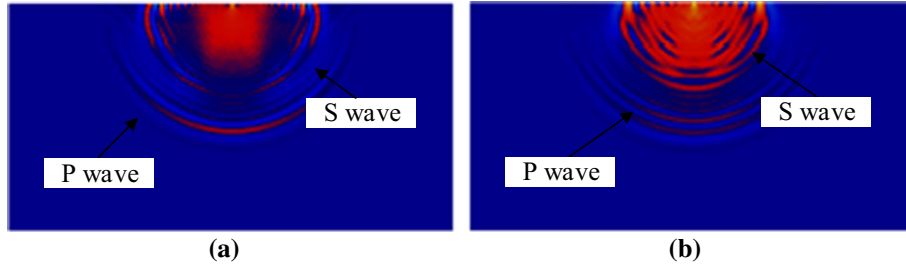


Fig. 9 Vertical displacement fields at $t = 4.0 \mu\text{s}$: **a** classical medium; **b** micro-polar medium

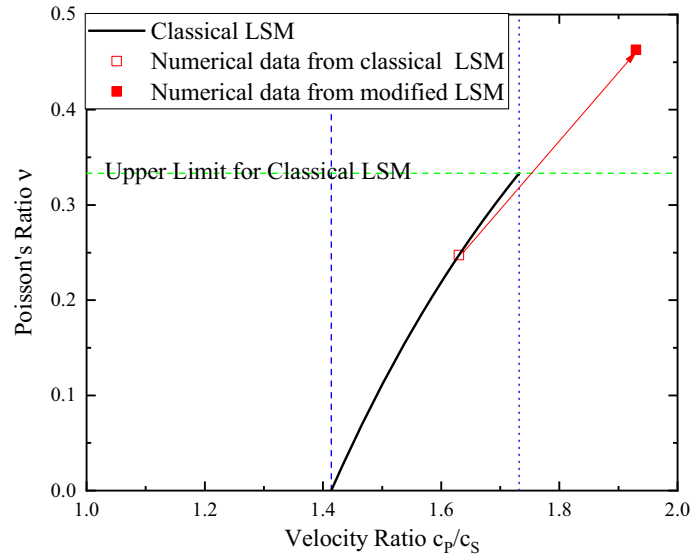


Fig. 10 Poisson’s ratio changing with respect to velocity ratio

This velocity ratio is also related to Poisson’s ratio, and for a two-dimensional (2D) isotropic elastic medium, we have

$$\lambda = \frac{E\nu}{1 - \nu^2}, \tag{73}$$

$$\mu = \frac{E}{2(1 + \nu)}, \tag{74}$$

and then

$$\left(\frac{c_p}{c_s}\right)^2 = \frac{2}{1 - \nu}, \tag{75}$$

where E and ν are Young’s modulus and Poisson’s ratio. Figure 10 displays the variation in the Poisson’s ratio with velocity ratio: The data obtained from classical LSM are about 0.247 (hollow square), and from modified LSM the data are about 0.463 (solid square), which increases by nearly 87.45% and larger than the upper limit $\frac{1}{3}$ for classical LSM in 2D by 39.03%. As shown in this figure, align with the available research [64], the nodal rotation could expand the range of Poisson’s ratio. It illustrates the necessity of considering the rotation of lattice nodes in the lattice model.

For a regularly arranged lattice model with the lattice node regarded as a uniformly distributed disk of radius of $\frac{d}{2}$, its moment of inertia about the perpendicular axis, the y axis, can be expressed as [37,48]

$$I_y^0 = \frac{1}{8}md^2. \tag{76}$$

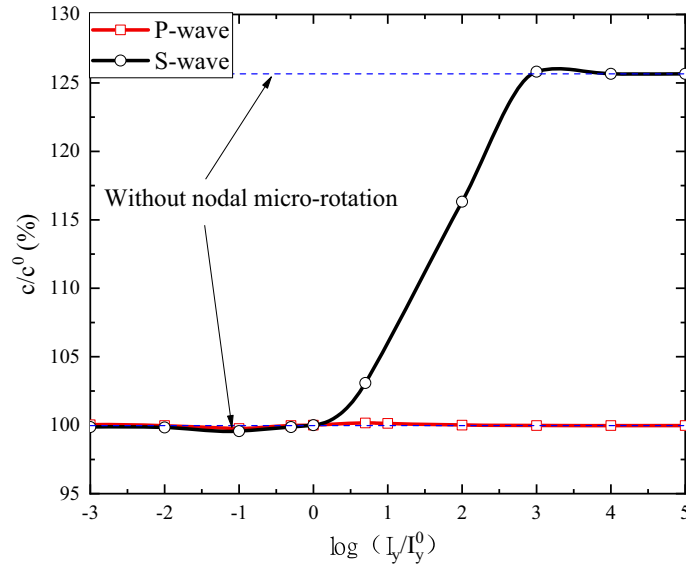


Fig. 11 Dimensionless velocities of P- and S-waves versus dimensionless micro-inertia (log) plot

We take this value as the reference and compute dimensionless velocities of P- and S-waves regarding different micro-rotational inertia. In Fig. 11, c^0 means the minimum value for P- or S-wave velocity. As shown in this figure, whether the rotation is considered or not, it makes little effect on the P-wave velocity, but a considerable effect on that of the S-wave, which is consistent with the theoretical prediction of Eqs. (26) and (30). With the micro-rotation inertia increasing up to 10^3 times that of the reference, the S-wave propagates faster, with its velocity tending to be stable approximately at the value of classical LSM. The modified LSMs show visible differences for the micro-rotation inertia falling within the range of 1 to 10^3 .

3.6 Parameter identification

For this modified LSM with a given lattice spacing d , numerical damping ζ and micro-rotational inertia I_y may influence the calculation precision as illustrated in Sects. 3.3–3.5. Additionally, Poisson’s ratio in this modified LSM is not only related to stiffness ratio ξ , but also the independent micro-rotational inertia I_y , which might be hardly represented by an exact expression. Thus, the Dakota toolkit [1, 32] is used for parameter identification.

Parameter identification is a significant step in numerical simulations, especially for those based on discrete concepts. Its essence is to solve the inverse problems. In this paper, the NL2SOL algorithm in Dakota analysis toolkit is used to minimize the residual of the objective function for the ‘optimal’ parameters. The objective function can be written as the sum of the least squares of the relative errors between simulation results and the given data as follows:

$$R(\mathbf{X}) = \sum_{i=1}^N \left(\frac{a_i(\mathbf{X}) - a_0}{a_0} \right)^2 + \sum_{i=1}^N \left(\frac{b_i(\mathbf{X}) - b_0}{b_0} \right)^2 + \dots, \tag{77}$$

with $\mathbf{X}_{\text{Lower}} \leq \mathbf{X} \leq \mathbf{X}_{\text{Upper}}$, where N is the number of target values; \mathbf{X} is the n -dimensional vector of the input parameters; $a_i(\mathbf{X})$ and $b_i(\mathbf{X})$ are the numerical data over the relevant experimental constants a_0 and b_0 . The specific calibration procedure for parameter identification is shown in Fig. 12.

To obtain the inputs for the given material listed in Table 1, the objective function in the NL2SOL algorithm is set to

$$R(\mathbf{X}) = \sum_{i=1}^N \left(\frac{\left(\frac{c_p}{c_s} \right)_i(\mathbf{X}) - \frac{c_p^0}{c_s^0}}{\frac{c_p^0}{c_s^0}} \right)^2, \tag{78}$$

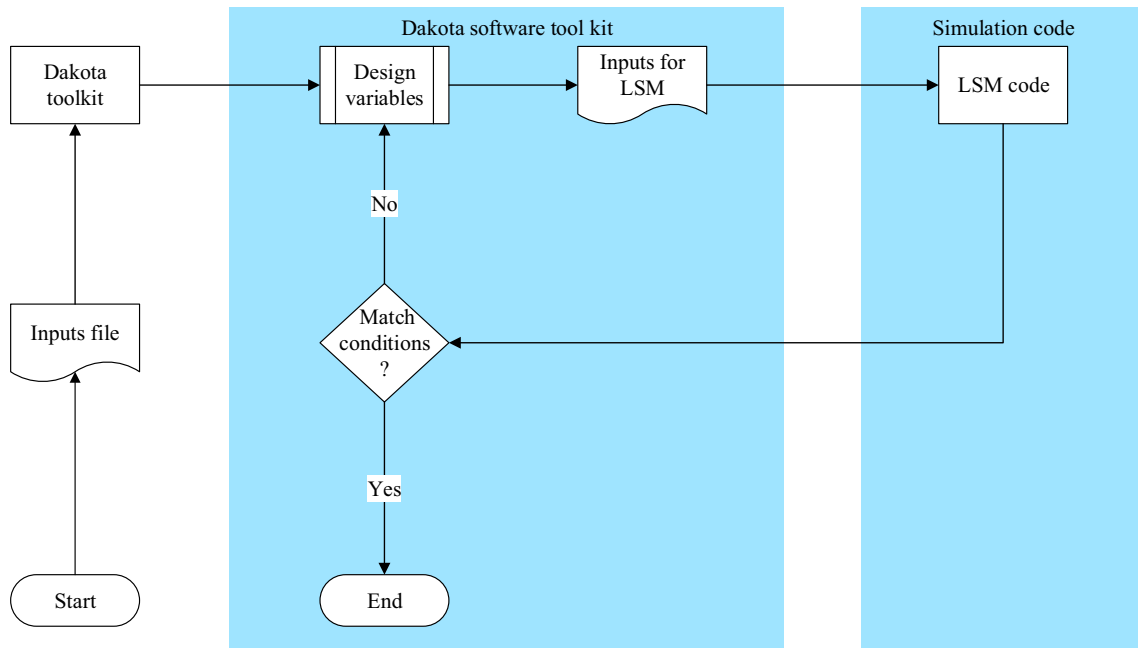


Fig. 12 Flowchart for parameter identification via Dakota toolkit

Table 1 Material parameters

Material	Elastic constants		Density $\rho/\text{kg/m}^3$	Theoretical velocities	
	C_{11}/GPa	C_{44}/GPa		$c_p/\text{m/s}$	$c_s/\text{m/s}$
Cooper	221.1	59.3	8970	4965	2572

Table 2 Inputs of mass node

Input parameter	d/mm	$m_{\text{node}}/\text{mg}$	$I_y/\text{mg} \cdot \text{mm}^2$	$K_n/\text{GPa} \cdot \text{m}$	$K_s/\text{GPa} \cdot \text{m}$	ζ
Input value	0.08	49.72	0.04	77.89	15.58	0.12

with $\mathbf{X} = (\zeta \ \xi \ I_y)$, where c_p^0 and c_s^0 are the theoretical P-wave and S-wave velocities at a given frequency, respectively.

In order to reduce the iterations, reasonable initial guess values and the lower and upper bounds should be chosen. We set the initial values and bounds of elastic constants according to Eqs. (66) and (72). After multiple iterations, the ‘best’ values under given objective functions for this modified LSM are obtained as displayed in Table 2.

4 Validation and verification for the LSM

This section aims to validate the implementation of the LSM described in the paper. For this purpose, the propagation problem of elastic waves in an isotropic medium is solved by the LSM without micro-rotation (namely the classical LSM) and the commercial FEM software (Nastran) [56, 58, 59] and a comparison is made between the two methods.

Firstly, we generate the lattice nodes within the domain as shown in Fig. 3 with the lattice spacing of 0.1mm, whereas the FEM meshing uses regular triangular elements by positioning mesh nodes according to the LSM lattice nodes. Then, we can set the lattice node inertia to a significant value to implement the classical LSM without the micro-rotation involved. The LSM uses input parameters shown in Table 2, with its optimal numerical damping ζ set to 0.06. The resulting vertical displacement fields at $t = 4.0 \mu\text{s}$ are shown in Fig.

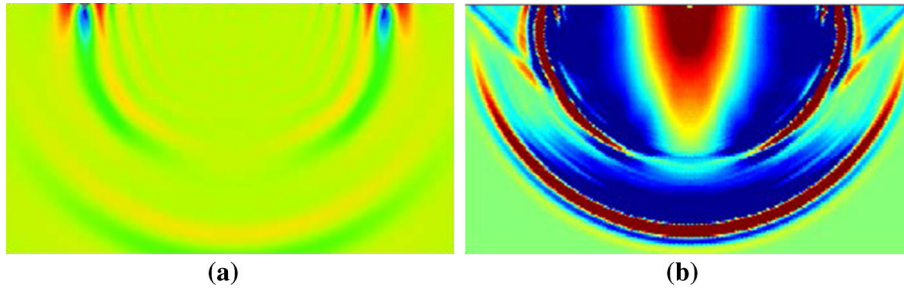


Fig. 13 Vertical displacement fields at $t = 4.0 \mu\text{s}$ by FEM (a) and LSM (b)

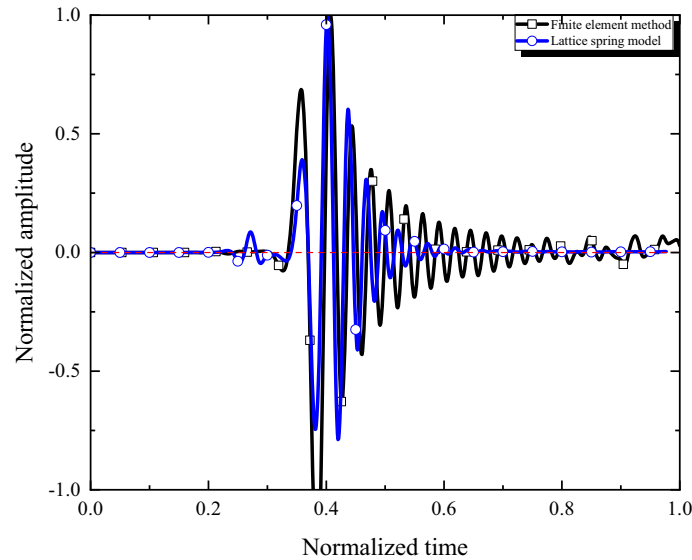


Fig. 14 Comparison of detailed variations between the vertical displacements at the same receiver with 10 mm from the source by FEM and LSM

13. We see that the P- and S-wave fronts can be observed clearly in both the numerical simulations, which indicates that the LSM scheme can simulate elastic wave propagation in an isotropic medium as well. Figure 14 compares detailed variations between the vertical displacements at the same receiver by these two methods. We see a generally consistent change between these curves, with some minor departures observed in amplitude. The waveforms by the LSM show more obvious characteristics with easier identification. In addition, the wave signal from the FEM has a long oscillation duration, which may affect the pickup of S-wave first arrivals. This may be attributed to lack of an adaptive damping in this FEM model. However, the dependences of the damping via FEM on the wave dispersion are beyond the scope of this paper, but would be an interesting topic for future studies.

5 Comparison of wave dispersion relations

To demonstrate the applicability of the modified LSM, numerical experiments are conducted using Ricker wavelets at various center frequencies for the model shown in Fig. 2 with the material parameters listed in Table 2, with comparison to theoretical values based on the classical continuum and modified couple stress theory [48].

Figure 15 shows angular frequencies changing with respect to normalized wave numbers of P- and S-waves, calculated by different methods for given frequencies. We see that the relation between the normalized P-wave number and the angular frequency could be fitted to a straight line for all the methods, modified LSM, and two kinds of theoretical predictions. It means that the P-wave velocity does not change with frequencies as expected theoretically. For the S-wave, the values calculated by classical continuum theory still exhibit a linear

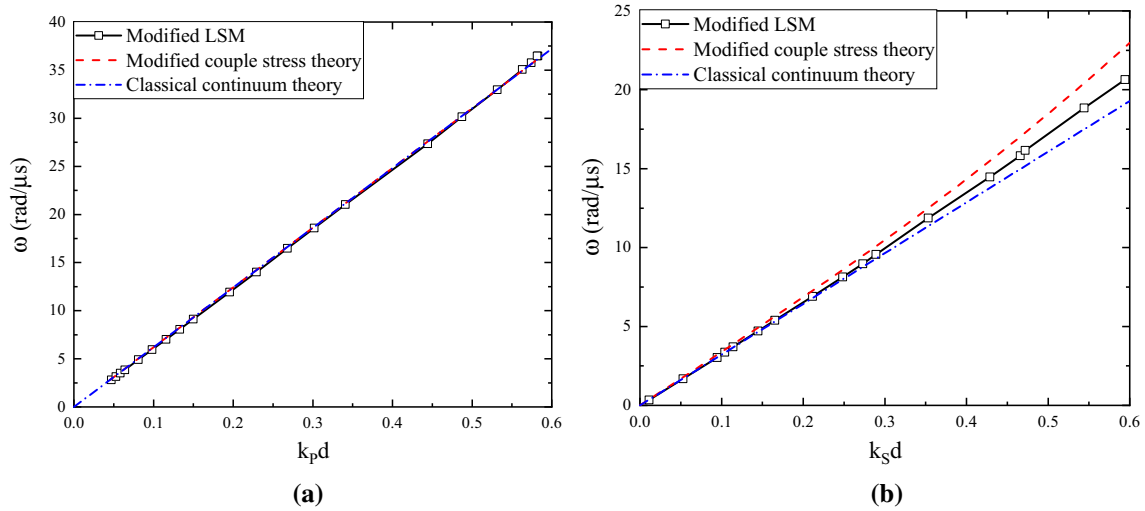


Fig. 15 Angular frequencies changing with respect to normalized wave numbers for P-wave (a) and S-wave (b)

relationship, indicating a non-dispersive behavior, whereas the normalized numerical curve by the modified LSM is nonlinear, with the relevant data fitted by Eq. (32). From these fitting parameters, we can estimate the characteristic material length, approximately $71.32 \mu\text{m}$. This value is nearly one third the shear wavelength of $218.19 \mu\text{m}$ at $\omega = 20.65 \text{ rad}/\mu\text{s}$. It is worth stressing that much longer shear wavelengths make the normalized wave number tend to zero, with the corresponding dispersion curve of the modified LSM reduced to that of the classical continuum theory. This performance of the modified LSM agrees with the analytical prediction mentioned in Sect. 2.2, where the couple stress effect could be ignored when the characteristic material length l is small relative to the wavelength. From this figure, we can also see that the S-wave velocity calculated by the modified LSM is higher than that of the classical continuum medium. Therefore, the S-wave velocity at high frequencies is generally underestimated by the conventional theory.

6 Conclusions and remarks

In this paper, a modified LSM is proposed by introducing an independent micro-rotational inertia obtained from a parameter identification process provided in the Dakota toolkit, which might help to characterize the size-dependent effect and model an isotropic material with a Poisson ratio larger than $\frac{1}{3}$ for 2D triangular lattices. By comparing with the modified couple stress theory, we analyze the dispersion relationship of elastic waves for the estimation of the characteristic material parameter. The main conclusions are summarized as follows:

1. For this modified LSM approach, stiffness ratio, numerical damping, lattice spacing, and micro-rotational inertia may influence the Poisson's ratio. For a given Poisson's ratio, the 'optimal' values could be obtained by the Dakota toolkit, when parts of those parameters are given.
2. A comparison is made between our scheme and the modified couple stress theory, which shows that the modified LSM could be used to emulate the size-dependent wave propagation and mimic the shear wave dispersion under high-frequency vibration.
3. Different source functions might affect the dispersion relations of elastic waves. By modified LSM modeling, it is verified that the Ricker wavelet is more suitable than the cosine function as a human-made excitation source.

Although this method may provide an alternative and promising way to investigate the size-dependent wave propagation in elastic media with a higher Poisson's ratio numerically, it is undeniable that further study is needed for emulating wave propagation in more complicated media.

Acknowledgements This work is financially supported by the Natural Science Foundation of China (Grant Nos. 41821002 and 41804134). We also would like to thank the editors and the anonymous reviewers for insightful feedbacks.

References

1. Adams, B.M., Bohnhoff, W., Dalbey, K., Eddy, J., Eldred, M., Gay, D., Haskell, K., Hough, P.D., Swiler, L.P.: Dakota, a multilevel parallel object-oriented framework for design optimization, parameter estimation, uncertainty quantification, and sensitivity analysis: version 5.0 user's manual. Sandia National Laboratories, Tech. Rep. SAND2010-2183 (2009)
2. Akbarzadeh Khorshidi, M., Shariati, M.: An investigation of stress wave propagation in a shear deformable nanobeam based on modified couple stress theory. *Waves Random Complex Media* **26**(2), 243–258 (2016)
3. Caldarelli, G., Castellano, C., Petri, A.: Criticality in models for fracture in disordered media. *Physica A* **270**(1–2), 15–20 (1999)
4. Chong, A., Yang, F., Lam, D., Tong, P.: Torsion and bending of micron-scaled structures. *J. Mater. Res.* **16**(4), 1052–1058 (2001)
5. Cosserat, E.: *Theorie des corps deformables*. Herman et fils Paris (1909)
6. Cundall, P.A., Strack, O.D.: A discrete numerical model for granular assemblies. *Geotechnique* **29**(1), 47–65 (1979)
7. Cusatis, G., Bažant, Z.P., Cedolin, L.: Confinement-shear lattice model for concrete damage in tension and compression: I. Theory. *J. Eng. Mech.* **129**(12), 1439–1448 (2003)
8. Damjanac, B., Detournay, C., Cundall, P.A.: Application of particle and lattice codes to simulation of hydraulic fracturing. *Comput. Part. Mech.* **3**(2), 249–261 (2016)
9. Del Valle-García, R., Sánchez-Sesma, F.J.: Rayleigh waves modeling using an elastic lattice model. *Geophys. Res. Lett.* **30**(16), SDE12. 1-SDE12. 4 (2003)
10. Eringen, A.C.: Mechanics of micromorphic continua. In: *Mechanics of Generalized Continua*, pp. 18–35. Springer (1968)
11. Gao, X.L., Huang, J., Reddy, J.: A non-classical third-order shear deformation plate model based on a modified couple stress theory. *Acta Mech.* **224**(11), 2699–2718 (2013)
12. Gholamy, A., Kreinovich, V.: Why ricker wavelets are successful in processing seismic data: towards a theoretical explanation. In: 2014 IEEE Symposium on Computational Intelligence for Engineering Solutions (CIES), pp. 11–16. IEEE (2014)
13. Griffiths, D., Mustoe, G.G.: Modelling of elastic continua using a grillage of structural elements based on discrete element concepts. *Int. J. Numer. Methods Eng.* **50**(7), 1759–1775 (2001)
14. Grubmüller, H., Heller, H., Windemuth, A., Schulten, K.: Generalized verlet algorithm for efficient molecular dynamics simulations with long-range interactions. *Mol. Simul.* **6**(1–3), 121–142 (1991)
15. Güven, U.: The investigation of the nonlocal longitudinal stress waves with modified couple stress theory. *Acta Mech.* **221**(3–4), 321–325 (2011)
16. Güven, U.: A more general investigation for the longitudinal stress waves in microrods with initial stress. *Acta Mech.* **223**(9), 2065–2074 (2012)
17. Güven, U.: Two mode Mindlin-Herrmann rod solution based on modified couple stress theory. *J. Appl. Math. Mech. Zeitschrift für Angewandte Mathematik und Mechanik (ZAMM)* **94**(12), 1011–1016 (2014)
18. Hadjesfandiari, A.R., Dargush, G.F.: Couple stress theory for solids. *Int. J. Solids Struct.* **48**(18), 2496–2510 (2011)
19. Hahn, M., Bouriga, M., Kröplin, B.H., Wallmersperger, T.: Life time prediction of metallic materials with the discrete-element-method. *Comput. Mater. Sci.* **71**, 146–156 (2013)
20. Hassold, G., Srolovitz, D.: Brittle fracture in materials with random defects. *Phys. Rev. B* **39**(13), 9273 (1989)
21. Ikelle, L.T., Amundsen, L.: *Introduction to Petroleum Seismology*. Society of Exploration Geophysicists, Tulsa (2018)
22. Jiang, C., Zhao, G.F.: Implementation of a coupled plastic damage distinct lattice spring model for dynamic crack propagation in geomaterials. *Int. J. Numer. Anal. Meth. Geomech.* **42**(4), 674–693 (2018)
23. Karihaloo, B.L., Shao, P., Xiao, Q.: Lattice modelling of the failure of particle composites. *Eng. Fract. Mech.* **70**(17), 2385–2406 (2003)
24. Kawai, T.: New discrete models and their application to seismic response analysis of structures. *Nucl. Eng. Des.* **48**(1), 207–229 (1978)
25. Khorshidi, M.A., Shariati, M.: Propagation of stress wave in a functionally graded nano-bar based on modified couple stress theory. *J. Mech. Eng. Technol. (JMET)* **7**(1), 43–56 (2015)
26. Koiter, W.: Couple-stress in the theory of elasticity. In: *Proc. K. Ned. Akad. Wet.*, vol. 67, pp. 17–44. North Holland Pub (1964)
27. Kumagai, H., Saito, T., O'Brien, G., Yamashina, T.: Characterization of scattered seismic wavefields simulated in heterogeneous media with topography. *J. Geophys. Res. Solid Earth* **116**(B3), B03308 (2011)
28. Li, G., Tang, G., Luo, G., Wang, H.: Underdetermined blind separation of bearing faults in hyperplane space with variational mode decomposition. *Mech. Syst. Signal Process.* **120**, 83–97 (2019)
29. Lilliu, G., van Mier, J.G.: 3D lattice type fracture model for concrete. *Eng. Fract. Mech.* **70**(7–8), 927–941 (2003)
30. Liu, H., Zhang, Y., Kang, W., Zhang, P., Duan, H., He, X.: Molecular dynamics simulation of strong shock waves propagating in dense deuterium, taking into consideration effects of excited electrons. *Phys. Rev. E* **95**(2), 023201 (2017)
31. Liu, J., Deng, S., Zhang, J., Liang, N.: Lattice type of fracture model for concrete. *Theor. Appl. Fract. Mech.* **48**(3), 269–284 (2007)
32. Liu, N., Li, M., Chen, W.: Mechanical deterioration of rock salt at different confinement levels: a grain-based lattice scheme assessment. *Comput. Geotech.* **84**, 210–224 (2017)
33. Liu, N., Wang, Y.G., Li, M., Jia, J.: Nonlinear buckling analyses of a small-radius carbon nanotube. *J. Appl. Phys.* **115**(15), 154301 (2014)
34. Ma, H., Gao, X.L., Reddy, J.: A microstructure-dependent timoshenko beam model based on a modified couple stress theory. *J. Mech. Phys. Solids* **56**(12), 3379–3391 (2008)
35. Ma, H., Gao, X.L., Reddy, J.: A non-classical Mindlin plate model based on a modified couple stress theory. *Acta Mech.* **220**(1–4), 217–235 (2011)
36. Matle, S.: Elastic wave propagation study in copper poly-grain sample using FEM. *Theor. Appl. Mech. Lett.* **7**(1), 1–5 (2017)
37. Meriam, J.L., Kraige, L.G.: *Engineering Mechanics: Dynamics*, vol. 2. Wiley, Hoboken (2012)
38. Mindlin, R., Tiersten, H.: Effects of couple-stresses in linear elasticity. *Arch. Ration. Mech. Anal.* **11**(1), 415–448 (1962)

39. Monette, L., Anderson, M.: Elastic and fracture properties of the two-dimensional triangular and square lattices. *Modell. Simul. Mater. Sci. Eng.* **2**(1), 53 (1994)
40. Mühlhaus, H., Oka, F.: Dispersion and wave propagation in discrete and continuous models for granular materials. *Int. J. Solids Struct.* **33**(19), 2841–2858 (1996)
41. Ostoja-Starzewski, M.: Lattice models in micromechanics. *Appl. Mech. Rev.* **55**(1), 35–60 (2002)
42. Ostoja-Starzewski, M., Sheng, P., Alzebdeh, K.: Spring network models in elasticity and fracture of composites and polycrystals. *Comput. Mater. Sci.* **7**(1–2), 82–93 (1996)
43. Otter, J.R.H., Cassell, A.C., Hobbs, R.E.: POISSON: dynamic relaxation. *Proc. Inst. Civ. Eng.* **35**(4), 633–656 (1966)
44. Park, S., Gao, X.: Bernoulli-euler beam model based on a modified couple stress theory. *J. Micromech. Microeng.* **16**(11), 2355 (2006)
45. Park, S., Gao, X.L.: Variational formulation of a modified couple stress theory and its application to a simple shear problem. *Zeitschrift für angewandte Mathematik und Physik* **59**(5), 904–917 (2008)
46. Reck, M.: Lattice spring methods for arbitrary meshes in two and three dimensions. *Int. J. Numer. Methods Eng.* **110**(4), 333–349 (2017)
47. Schlangen, E., Garboczi, E.: Fracture simulations of concrete using lattice models: computational aspects. *Eng. Fract. Mech.* **57**(2–3), 319–332 (1997)
48. Suiker, A., Metrikine, A., De Borst, R.: Comparison of wave propagation characteristics of the Cosserat continuum model and corresponding discrete lattice models. *Int. J. Solids Struct.* **38**(9), 1563–1583 (2001)
49. Toomey, A., Bean, C.J.: Numerical simulation of seismic waves using a discrete particle scheme. *Geophys. J. Int.* **141**(3), 595–604 (2000)
50. Toupin, R.A.: Elastic materials with couple-stresses. *Arch. Ration. Mech. Anal.* **11**(1), 385–414 (1962)
51. Voigt, W.: Ueber die beziehung zwischen den beiden elasticitätsconstanten isotroper körper. *Ann. Phys.* **274**(12), 573–587 (1889)
52. Wang, Y.G., Lin, W.H., Liu, N.: Large amplitude free vibration of size-dependent circular microplates based on the modified couple stress theory. *Int. J. Mech. Sci.* **71**, 51–57 (2013)
53. Wang, Y.G., Lin, W.H., Liu, N.: Nonlinear free vibration of a microscale beam based on modified couple stress theory. *Physica E* **47**, 80–85 (2013)
54. Wang, Y.G., Lin, W.H., Liu, N.: Nonlinear bending and post-buckling of extensible microscale beams based on modified couple stress theory. *Appl. Math. Model.* **39**(1), 117–127 (2015)
55. Xia, M., Zhou, H., Chen, H., Zhang, Q., Li, Q.: A rectangular-grid lattice spring model for modeling elastic waves in poisson's solids. *Geophysics* **83**(2), T69–T86 (2018)
56. Yang, C., Hou, X., Wang, L.: Thermal design, analysis and comparison on three concepts of space solar power satellite. *Acta Astronaut.* **137**, 382–402 (2017)
57. Yang, C., Liang, K., Zhang, X., Geng, X.: Sensor placement algorithm for structural health monitoring with redundancy elimination model based on sub-clustering strategy. *Mech. Syst. Signal Process.* **124**, 369–387 (2019)
58. Yang, C., Lu, Z., Yang, Z.: Robust optimal sensor placement for uncertain structures with interval parameters. *IEEE Sens. J.* **18**(5), 2031–2041 (2018)
59. Yang, C., Zhang, X., Huang, X., Cheng, Z., Zhang, X., Hou, X.: Optimal sensor placement for deployable antenna module health monitoring in SSPS using genetic algorithm. *Acta Astronaut.* **140**, 213–224 (2017)
60. Yang, F., Chong, A., Lam, D.C.C., Tong, P.: Couple stress based strain gradient theory for elasticity. *Int. J. Solids Struct.* **39**(10), 2731–2743 (2002)
61. Yang, L., Lobkis, O., Rokhlin, S.: An integrated model for ultrasonic wave propagation and scattering in a polycrystalline medium with elongated hexagonal grains. *Wave Motion* **49**(5), 544–560 (2012)
62. Zhang, G., Gao, X.L.: A non-classical kirchhoff rod model based on the modified couple stress theory. *Acta Mech.* **230**(1), 243–264 (2019)
63. Zhang, P., Wei, P., Li, Y.: Wave propagation through a micropolar slab sandwiched by two elastic half-spaces. *J. Vib. Acoust.* **138**(4), 041008 (2016)
64. Zhao, G.F., Fang, J., Sun, L., Zhao, J.: Parallelization of the distinct lattice spring model. *Int. J. Numer. Anal. Methods Geomech.* **37**(1), 51–74 (2013)
65. Zhao, G.F., Fang, J., Zhao, J.: A 3D distinct lattice spring model for elasticity and dynamic failure. *Int. J. Numer. Anal. Methods Geomech.* **35**(8), 859–885 (2011)
66. Zubelewicz, A., Bažant, Z.P.: Interface element modeling of fracture in aggregate composites. *J. Eng. Mech.* **113**(11), 1619–1630 (1987)